

Enhanced continuous-wave four-wave mixing efficiency in nonlinear AlGaAs waveguides

Paveen Apiratikul,^{1,2,*} Jeremiah J. Wathen,^{1,2} Gyorgy A. Porkolab,^{1,2}
Bohan Wang,¹ Lei He,^{1,2} Thomas E. Murphy,^{1,2}
and Christopher J. K. Richardson²

¹University of Maryland, College Park, MD 20742, USA

²Laboratory for Physical Sciences, College Park, MD 20740, USA

*paveen@lps.umd.edu

Abstract: Enhancements of the continuous-wave four-wave mixing conversion efficiency and bandwidth are accomplished through the application of plasma-assisted photoresist reflow to reduce the sidewall roughness of sub-square-micron-modal area waveguides. Nonlinear AlGaAs optical waveguides with a propagation loss of 0.56 dB/cm demonstrate continuous-wave four-wave mixing conversion efficiency of -7.8 dB. Narrow waveguides that are fabricated with engineered processing produce waveguides with uncoated sidewalls and anti-reflection coatings that show group velocity dispersion of +0.22 ps²/m. Waveguides that are 5-mm long demonstrate broadband four-wave mixing conversion efficiencies with a half-width 3-dB bandwidth of 63.8-nm.

© 2014 Optical Society of America

OCIS codes: (190.4380) Nonlinear optics, four-wave mixing; (160.4330) Nonlinear optical materials; (190.5970) Semiconductor nonlinear optics; (230.7370) Waveguides; (190.4390) Nonlinear optics, integrated optics; (230.4320) Nonlinear optical devices.

References and links

1. J. H. Lee, W. Belardi, K. Furusawa, P. Petropoulos, Z. Yusoff, T. M. Monro, and D. J. Richardson, "Four-wave mixing based 10-Gb/s tunable wavelength conversion using a holey fiber with a high SBS threshold," *IEEE Photon. Technol. Lett.* **15**, 440–442 (2003).
2. X. Yang, A. K. Mishra, R. J. Manning, R. P. Webb, and A. D. Ellis, "All-optical 42.6 Gbit/s NRZ to RZ format conversion by cross-phase modulation in single SOA," *Electron. Lett.* **43**, 890–892 (2007).
3. E. C. Mägi, L. B. Fu, H. C. Nguyen, M. R. E. Lamont, D. I. Yeom, and B. J. Eggleton, "Enhanced Kerr nonlinearity in sub-wavelength diameter As₂Se₃ chalcogenide fiber tapers," *Opt. Express* **15**, 10324–10329 (2007).
4. M. A. Foster, A. C. Turner, R. Salem, M. Lipson, and A. L. Gaeta, "Broad-band continuous-wave parametric wavelength conversion in silicon nanowaveguides," *Opt. Express* **15**, 12949–12958 (2007).
5. W. Mathlouthi, H. Rong, and M. Paniccia, "Characterization of efficient wavelength conversion by four-wave mixing in sub-micron silicon waveguides," *Opt. Express* **16**, 16735–16745 (2008).
6. B. Kuyken, S. Clemmen, S. K. Selvaraja, W. Bogaerts, D. V. Thourhout, P. Emplit, S. Massar, G. Roelkens, and R. Baets, "On-chip parametric amplification with 26.5 dB gain at telecommunication wavelengths using CMOS-compatible hydrogenated amorphous silicon waveguides," *Opt. Lett.* **20**, 4085–4101 (2011).
7. K.-Y. Wang and A. C. Foster, "Ultralow power continuous-wave frequency conversion in hydrogenated amorphous silicon waveguides," *Opt. Lett.* **37**, 1331–1333 (2012).
8. S. Suda, K. Tanizawa, Y. Sakakibara, T. Kamei, K. Nakanishi, I. Itoga, T. Ogasawara, R. Takei, K. Kawashima, S. Namiki, M. Mori, T. Hasama, and K. Ishikawa, "Pattern-effect-free all-optical wavelength conversion using hydrogenated amorphous silicon waveguide with ultra-fast carrier decay," *Opt. Lett.* **37**, 1382–1384 (2012).
9. P. Apiratikul, W. Astar, G. M. Carter, and T. E. Murphy, "Demonstration of 10-Gb/s wavelength conversion using four-wave mixing in GaAs waveguide," *IEEE Photon. Technol. Lett.* **22**, 872–874 (2010).

10. K. Dolgaleva, W. C. Ng, L. Qian, and J. S. Aitchison, "Compact highly-nonlinear AlGaAs waveguides for efficient wavelength conversion," *Opt. Express* **19**, 12440–12455 (2011).
11. B. M. Cannon, T. Mahmood, W. Astar, P. Apiratikul, G. Porkolab, P. Boudra, T. Mohsenin, C. J. K. Richardson, and G. M. Carter, "All-optical amplitude-phase transmultiplexing of RZ-OOK and RZ-BPSK to RZ-QPSK by polarization-insensitive XPM using a nonlinear birefringent AlGaAs waveguide," *Opt. Express* **21**, 19885–19899 (2013).
12. L. Jia, M. Geng, L. Zhang, L. Yang, P. Chen, Y. Liu, Q. Fang, and M. Yu, "Effects of waveguide length and pump power on the efficiency of wavelength conversion in silicon nanowire waveguides," *Opt. Lett.* **34**, 3502–3504 (2009).
13. J. S. Aitchison, D. C. Hutchings, J. U. Kang, G. I. Stegeman, and A. Villeneuve, "The nonlinear optical properties of AlGaAs at the half band gap," *IEEE J. Quantum Electron.* **33**, 341–348 (1987).
14. M. Dinu, F. Quochi, and H. Garcia, "Third-order nonlinearities in silicon at telecom wavelengths," *Appl. Phys. Lett.* **82**, 2955–2957 (2003).
15. G. A. Siviloglou, S. Sunstov, R. El-Ganainy, R. Iwanow, G. I. Stegeman, and D. N. Christodoulides, "Enhanced third-order nonlinear effects in optical AlGaAs nanowires," *Opt. Express* **14**, 9377–9384 (2006).
16. C. Lacava, V. Pusino, P. Minzioni, M. Sorel, and I. Cristiani, "Nonlinear properties of AlGaAs waveguides in continuous wave operation regime," *Opt. Express* **22**, 5291–5297 (2014).
17. J. Meier, W. S. Mohammed, A. Jugessur, L. Qian, M. Mojahedi, and J. S. Aitchison, "Group velocity inversion in AlGaAs nanowires," *Opt. Express* **15**, 12755–12762 (2007).
18. G. A. Porkolab, P. Apiratikul, S. H. Guo, and C. J. K. Richardson, "Low propagation loss AlGaAs waveguides fabricated with plasma-assisted photoresist reflow," *Opt. Express* **22**, 7733–7743 (2014).
19. X. Liu, W. M. J. Green, X. Chen, I. W. Hsieh, J. I. Dadap, Y. A. Vlasov, and R. M. Osgood, Jr., "Conformal dielectric overlayers for engineering dispersion and effective nonlinearity of silicon nanophotonic wires," *Opt. Lett.* **33**, 2889–2891 (2008).
20. A. B. Fallahkhair, K. S. Li, and T. E. Murphy, "Vector finite difference modesolver for anisotropic dielectric waveguides," *J. Lightwave Technol.* **26**, 1423–1431 (2008).
21. E. Kapon and R. Bhat, "Low-loss single-mode GaAs/AlGaAs optical waveguides grown by organometallic vapor phase epitaxy," *Appl. Phys. Lett.* **50**, 1628–1630 (1987).
22. J. R. Ong, R. Kumar, R. Aguinaldo, and S. Mookherjea, "Efficient CW four-wave mixing in silicon-on-insulator micro-rings with active carrier removal," *IEEE Photon. Technol. Lett.* **25**, 1699–1702 (2013).
23. M. Sheik-Bahae, D. C. Hutchings, D. J. Hagan, and E. W. Van Stryland, "Dispersion of bound electron nonlinear refraction in solids," *IEEE J. Quantum Electron.* **27**, 1296–1309 (1991).
24. J. J. Wathen, V. R. Pagan, and T. E. Murphy, "Simple method to characterize nonlinear refraction and loss in optical waveguides," *Opt. Lett.* **37**, 4693–4695 (2012).
25. J. J. Wathen, P. Apiratikul, C. J. K. Richardson, G. A. Porkolab, G. M. Carter, and T. E. Murphy, "Efficient continuous-wave four-wave mixing in bandgap-engineered AlGaAs waveguides," *Opt. Lett.* **39**, 3161–3164 (2014).
26. A. M. Darwish, E. P. Ippen, H. Q. Le, J. P. Donnelly, and S. H. Groves, "Optimization of four-wave mixing conversion efficiency in the presence of nonlinear loss," *Appl. Phys. Lett.* **69**, 737–739 (1996).
27. A. C. Turner, C. Manolatou, B. S. Schmidt, M. Lipson, M. A. Foster, J. E. Sharping, and A. L. Gaeta, "Tailored anomalous group-velocity dispersion in silicon channel waveguides," *Opt. Express* **14**, 4357–4362 (2006).
28. K. Inoue and T. Mukai, "Signal wavelength dependence of gain saturation in a fiber optical parametric amplifier," *Opt. Lett.* **26**, 10–12 (2001).

1. Introduction

The trend of increasing spectral efficiency in modern optical communication systems leads to improved data bandwidth and higher power consumption requirements for signal routing operations such as wavelength conversion and demultiplexing. Nonlinear optics offers an all-optical alternative to optical-electrical-optical based solutions that may one day offer competitive advantages as data densities and rates continue to increase. Several waveguide materials have been used to demonstrate all-optical signal processing capabilities at telecom wavelengths such as nonlinear fiber [1], semiconductor optical amplifiers [2], chalcogenide glass waveguides [3], crystalline and amorphous silicon nanowire waveguides [4–8], and GaAs and AlGaAs semiconductor waveguides [9–11].

Comparisons of these materials in light of all-optical signal processing performance focuses on the assessment of material parameters important to nonlinear cross-phase modulation (XPM) and four-wave mixing (FWM). Both of these processes are dependent on the nonlinear index

and they are degraded by two-photon absorption (TPA) and free-carrier effects that can also be induced by TPA [12]. This problem can be significantly mitigated by using materials with a bandgap energy that is engineered to be at least twice the photon energy.

While desirable for a number of reasons, such as the promise of mass production cost-efficiency and maturity of standard complementary-metal-oxide-semiconductor (CMOS) fabrication techniques, photonic devices composed of crystalline silicon are an alluring and obvious choice for nonlinear optical processing. However, crystalline silicon suffers from unavoidable TPA and associated free-carrier effects at telecom wavelengths. AlGaAs is an attractive alternative for semiconductor nonlinear waveguide because the AlGaAs bandgap can be optimized to minimize the effects of TPA throughout the telecommunication C-band [13]. Moreover, the optical Kerr coefficient, n_2 , of AlGaAs is approximately 500 times larger than that of standard fiber, and 2 times larger than that of crystalline silicon [14]. Several groups have demonstrated optical signal processing based on the third-order nonlinear effects in AlGaAs waveguides [10, 11, 15, 16]. Despite the strong Kerr nonlinearity and broadband transparency throughout the communication band of AlGaAs, these waveguides are usually fabricated in smaller cleanrooms that do not maintain photolithography tools that can compete with those in commercial CMOS foundries in terms of feature size and line edge roughness. Therefore, the nonlinear performance of these waveguides are typically limited by waveguide width, and propagation loss resulting from photolithographic limitations of the installed tools. Fabrication limits are especially evident for sub-micron scale high-index contrast waveguides that are required for high efficiency and low group velocity dispersion (GVD). Although an AlGaAs waveguide with anomalous GVD was reported [17], its application is limited by the high propagation loss of 80 dB/cm [15] resulting from scattering loss from the waveguide sidewall roughness.

FWM conversion efficiency is an important metric for comparing the nonlinear performance of different waveguides. While the FWM conversion efficiency can be measured using pump pulses [10], it is more accurate to determine the nonlinear characteristics of AlGaAs waveguides in the continuous wave (CW) regime because there are no additional uncertainties related to temporal profile of the input pulses

In this paper, waveguides that show a high CW FWM conversion efficiency and large bandwidth are reported. Connection to the design and fabrication process is completed by examining the impact of implementing the plasma-assisted photoresist reflow described in [18] and selective removal of the conformal dielectric coatings that is necessary to produce anti-reflection coatings on the input and output facets.

2. Waveguide fabrication

The waveguide epitaxial structure is grown using solid-source molecular beam epitaxy (MBE) on a n-doped GaAs substrate. As shown in Fig. 1, the epilayer heterostructure consists of a 0.8- μm -thick $\text{Al}_{0.18}\text{Ga}_{0.82}\text{As}$ core layer surrounded by a 0.2- μm -thick $\text{Al}_{0.7}\text{Ga}_{0.3}\text{As}$ upper cladding and a 2- μm -thick $\text{Al}_{0.7}\text{Ga}_{0.3}\text{As}$ lower cladding. The core layer is designed to have an energy bandgap of 1.64 eV in order to suppress TPA within the C-band. The waveguides are defined by projection lithography using positive i-line photoresist. The photoresist is smoothed after development using nitrogen plasma-assisted reflow [18]. This process is able to smooth the sidewall roughness of the photoresist with little lateral spread of the photoresist. The reflowed photoresist is then used as the etch mask in an inductively coupled plasma (ICP) etch to produce dual-channel ridge waveguides using a BCl_3 and N_2 gas mixture. The waveguides are cleaved to length and then coated with a conformal silicon nitride (SiN_x) layer that is deposited on both facets and the sidewalls of the waveguides via plasma-enhanced chemical vapor deposition. The SiN_x acts as a single layer anti reflection coating that reduces the facet reflection to less than 1×10^{-2} . It is known that conformal silicon nitride coating increase the net dispersion [19]. To

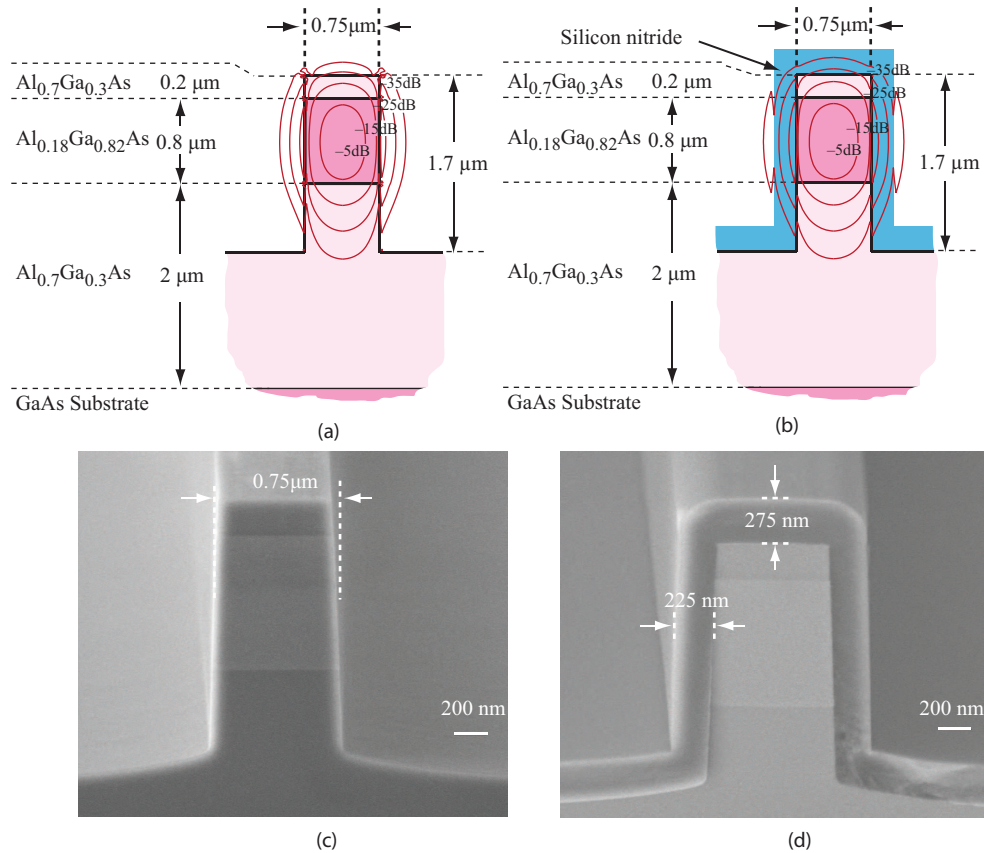


Fig. 1. Schematic cross-section superposed by the calculated fundamental TE mode contours of (a) uncoated and (b) coated AlGaAs waveguides. (c) and (d) show cross-sectional scanning electron micrograph of uncoated and coated 0.75- μm wide deep-etch AlGaAs waveguides.

determine the impact on these waveguides, the facets of some AlGaAs waveguides are protected with photoresist, and the silicon nitride is removed from the waveguide sidewalls using an oxygen plasma. Figure 1(a) depicts a 0.75- μm wide AlGaAs ridge waveguide superposed by the calculated transverse electric (TE) mode contours for uncoated waveguides, and Fig. 1(b) shows the same for a similar waveguide coated with a conformal layer of SiN_x . The nonlinear effective area A_{eff} is given by

$$A_{\text{eff}} = \frac{[\int_{-\infty}^{\infty} E(x,y)^2 dx dy]^2}{\int_{-\infty}^{\infty} E(x,y)^4 dx dy}, \quad (1)$$

where $E(x,y)$ is the electric field profile of the fundamental mode of the waveguide. The nonlinear effective area of the uncoated waveguide is estimated to be $0.44 \mu\text{m}^2$, and $0.47 \mu\text{m}^2$ for the coated waveguide, determined from a full-vector finite-difference calculation [20]. The cross-sectional scanning electron micrograph of the uncoated and coated AlGaAs ridge waveguides are also shown in Fig. 1(c) and Fig. 1(d), respectively.

For the presented waveguides, the optical loss primarily results from scattering loss due to the sidewall roughness. For i-line photolithographic processes that are optimized to achieve small

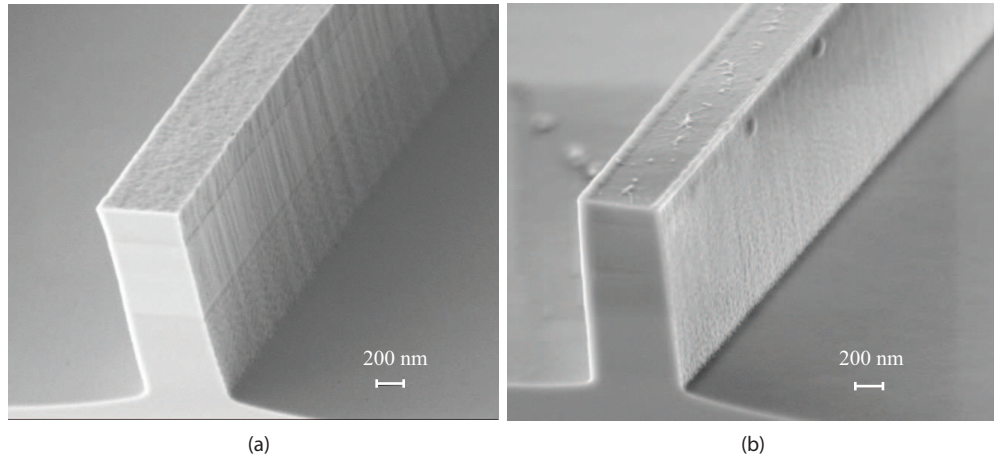


Fig. 2. Scanning electron micrographs of etched waveguides patterned by (a) as-developed and (b) plasma-assisted reflow photoresist processes. Reduction of the deep-etched sidewall roughness is evident in the plasma-assisted photoresist reflow process without significant relaxation of the waveguide width.

feature sizes, the sidewall roughness is an inherent artifact of the photolithographic chemistry and represents the ultimate line edge roughness that is achievable with a particular photochemistry. The vertical striations on the sidewalls of waveguides patterned by conventional photoresist processing is shown in Fig. 2(a) and demonstrates the texture that is transferred to the ridge sidewall during the ICP etch. In contrast, Fig. 2(b) shows an AlGaAs waveguide produced with the plasma-assisted reflow process producing much smoother waveguide sidewalls. The sidewall roughness reduction is confirmed by the line edge profile extracted from the plan-view SEM images of waveguide sidewalls. The RMS sidewall roughness is reduced from 3.4 nm for the as-developed photoresist waveguide to 1.4 nm for the plasma-assisted photoresist reflow waveguide.

3. Continuous-wave four-wave mixing efficiency

Figure 3 shows the experimental setup used to evaluate the conversion efficiency of these waveguides. Pump and signal beams are generated from two CW lasers with wavelengths of 1552.5 nm and 1551.9 nm. Both pump and signal beams are combined along the same polarization axis and coupled to the waveguide using polarization maintaining fibers, splitters, and lensed fibers to excite only the TE mode of the waveguide. The wavelength spacing between the pump and signal beams are less than 1 nm in order to minimize group-velocity mismatch among the interacting waves. A tap coupler is used at the input and the output of the waveguide to monitor the optical spectra and power coming in and out of the waveguide.

The 1.2- μm -wide waveguide, corresponding to an effective area of 0.72 μm^2 is patterned by as-developed photoresist, while the 1.35- μm -wide waveguide, which has an effective area of 0.83 μm^2 , is patterned by reflowed photoresist. Although both waveguides are originally patterned by the same photoresist width, the reflowed photoresist waveguide is slightly wider due to lateral spreading of patterned photoresist during the photoresist reflow process. The propagation loss of the waveguides is measured prior to applying the anti-reflection coating using the Fabry-Pérot technique [21]. The reflowed photoresist waveguide has smoother sidewalls, resulting in a lower TE-polarized propagation loss of 0.56 dB/cm, compared to that of the as-developed photoresist waveguide which is measured to be 1.90 dB/cm.

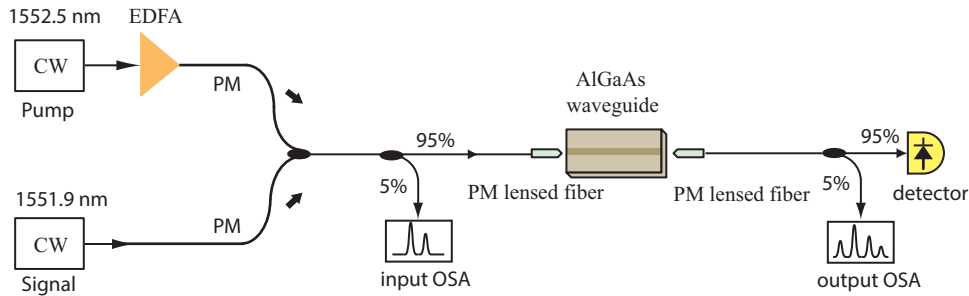


Fig. 3. Experimental setup for measuring CW-FWM conversion efficiency in AlGaAs waveguides.

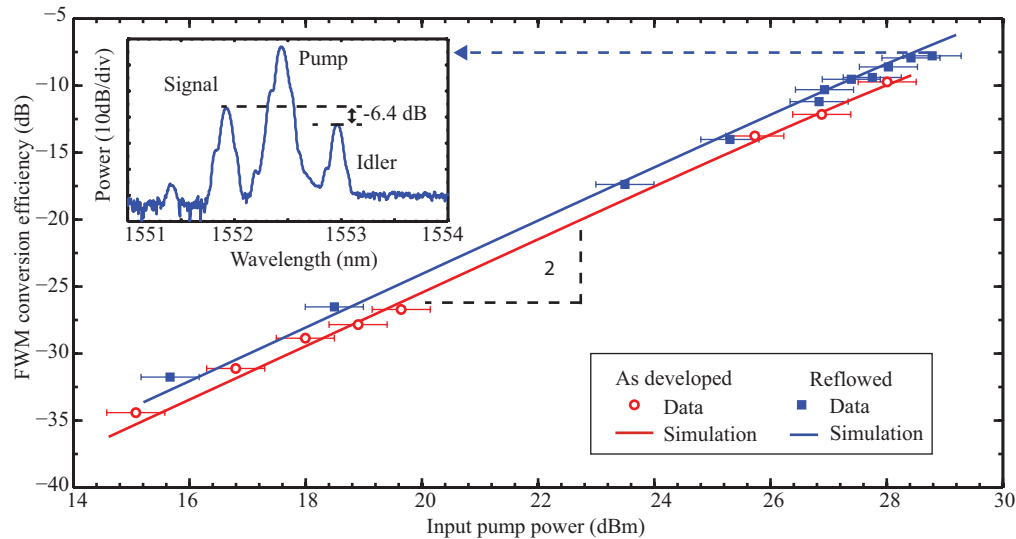


Fig. 4. Comparison of measured TE-polarized CW FWM conversion efficiency as a function of coupled input pump power of 2.5-cm long AlGaAs waveguides patterned by as-developed photoresist and by plasma-assisted reflowed photoresist. The inset shows the FWM output spectrum measured after AlGaAs waveguide fabricated using the plasma-assisted reflow process with a coupled input pump power of 29 dBm.

A comparison of the measured CW-FWM conversion efficiency for both 2.5-cm long waveguides as a function of the input pump power is shown in Fig. 4. The data for the waveguide fabricated with the as-developed photoresist process is depicted with open red circles and the efficiency of the waveguide fabricated with the reflowed photoresist process is depicted by the filled blue squares. FWM conversion efficiencies of both waveguides are proportional to the square of the input pump power as evidenced by the slope of 2 when the data is plotted on logarithmic-scale axes. In our experiment, the maximum coupled input pump power is limited to 29 dBm by optical damage to the waveguide input facet. The lack of saturation in Fig. 4 indicates that the TPA values are negligibly small for these experimental conditions.

The inset of Fig. 4 depicts the output spectrum from the waveguide patterned with the reflowed photoresist at the coupled input pump power of 29 dBm, showing the ratio of the output idler power to the output signal power to be -6.4 dB. This ratio includes propagation loss to the pump, signal and idler. Because saturation is not observed in Fig. 4, it is reasonable to neglect

the nonlinear loss of the waveguide. Therefore, the loss experienced by each beam propagating through the waveguide is determined by the linear loss in the waveguide, which is measured to be -1.4 dB. The FWM conversion efficiency, defined as a ratio of output idler to the input signal is -7.8 dB, which is determined by the measured output ratio (-6.4 dB) plus the linear loss of the signal beam (-1.4 dB). The FWM conversion efficiency in our waveguide is among the highest CW-FWM conversion efficiency reported in any semiconductor waveguides [5, 22], and represents a conservative estimate of the conversion efficiency in light of uncertainty in the partitioning of the input and output coupling losses. It is important to note that the waveguides are fabricated from different wafers, with slightly different bandgap energies, which results in a slightly lower n_2 for the waveguide that is fabricated with the plasma-assisted reflow process. At these input powers there is no evidence of nonlinear absorption nor subsequent free-carrier absorption that can cause a saturation of the FWM efficiency in either devices.

For cases such as this, where the pump is depleted by only linear loss, and the pump-signal wavelength detuning is small, the FWM conversion efficiency, η , can be solved analytically as

$$\eta = \frac{P_i(out)}{P_s(in)} = \exp(-\alpha L) \left(\frac{2\pi n_2}{\lambda A_{eff}} P_p(in) L_{eff} \right)^2 \quad (2)$$

where P_i , $i = \{p, s, i\}$ represent the powers of the pump, signal, and idler waves; α is the propagation loss; A_{eff} is the effective area of the waveguide; λ is the center wavelength; L is a waveguide length; and L_{eff} is the effective length that is defined as $[1 - \exp(-\alpha L)] / \alpha$.

From this analysis, the optical Kerr coefficients are extracted by fitting the data in Fig. 4 combined with measurements of the linear loss, and calculated effective area. These coefficients are $n_2 = 1.1 \times 10^{-4}$ cm²/GW for the as-developed-photoresist waveguide and $n_2 = 0.7 \times 10^{-4}$ cm²/GW for the plasma-reflowed-photoresist waveguide. This difference in n_2 , is consistent with the calculated change [23] based on the aluminum content of both wafers as measured by x-ray diffraction and verified with photoluminescence. It is evident that the FWM conversion efficiency in the waveguide made with the reflowed photoresist overcomes the higher optical Kerr coefficient of the waveguide patterned by the as-developed photoresist because of the reduction in the linear propagation loss. For completeness, these parameters are provided in Table 1.

Table 1. Parameters used to calculate the FWM conversion efficiencies shown in Fig. 4

Parameter	As-deposited	Plasma-reflowed
α (dB/cm)	1.91	0.56
α_2 (cm/GW)	0.05	0.03
n_2 (cm ² /GW)	1.1×10^{-4}	0.7×10^{-4}
A_{eff} (μm^2)	0.73	0.82
L (cm)	2.5	2.5

Separately, the nonlinear loss tangent technique [24] is used to determine the ratio of the imaginary part, γ_i , to the real part, γ_r , of the nonlinear parameters. For both waveguides, $\gamma_i/\gamma_r = 0.006 \pm 0.002$. The direct measurement of TPA coefficients using nonlinear transmission measurements shows that TPA coefficients of both waveguide-materials are below the detection limit of our experimental apparatus [25]. Combining the nonlinear loss tangent, and the extracted optical Kerr coefficients of these waveguides enables estimation of an upper bound of the TPA coefficients to be 0.05 cm/GW for the as-developed-photoresist waveguide and 0.03 cm/GW for the plasma-reflowed-photoresist waveguide. Because the TPA is negligibly small, the optimal waveguide length for FWM conversion efficiency L_{opt} only depends on the propagation loss of the waveguide as $\ln(3)/\alpha$ [26]. With this analysis, the plasma-assisted reflow

waveguide has an optimal length of 8.5 cm long, that is significantly longer than the fabricated waveguides. Using the optimal length, the same conversion efficiency could be achieved at less than half of the pump power, or a higher FWM conversion efficiency would be realized when pumped to the same level.

4. Continuous-wave four-wave mixing bandwidth

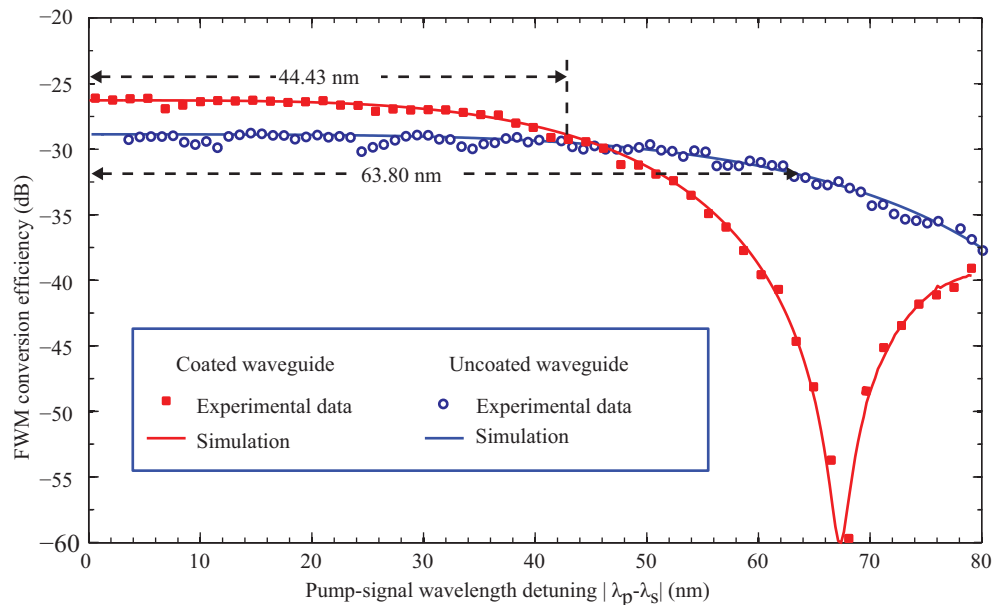


Fig. 5. Measured and simulated conversion efficiency as a function of pump-signal wavelength detuning for the fundamental TE mode in a $0.69 \mu\text{m}$ -wide waveguide before and after the SiN_x has been removed from the waveguide sidewalls. After removing the SiN_x on the sidewall, the waveguide has a larger bandwidth indicating a lower group velocity dispersion.

To achieve large FWM conversion bandwidths, the GVD needs to be to be near-zero or anomalous. For tightly confining sub-micron-area AlGaAs waveguides, the modal contribution to the net dispersion dominates that of the intrinsic dispersion of the materials in the waveguide. This allows adjusting the net dispersion by engineering the waveguide-geometry. [17, 27].

Figure 5 shows the TE-polarized FWM conversion efficiency as a function of pump-signal wavelength detuning for a $0.69\text{-}\mu\text{m}$ wide and 5-mm long waveguide before and after the SiN_x has been removed from the waveguide sidewalls while leaving the anti-reflection coatings intact on the input and output facets. In these experiments, the pump wavelength λ_p is fixed at 1550.4 nm, and the signal wavelength λ_s varies from 1551 nm to 1630 nm as limited by the laser tuning range. The half-width 3-dB conversion bandwidth is measured to be 44.4 nm for the coated waveguide, and 63.8 nm for the waveguide with the SiN_x removed.

The solid lines in Fig. 5 show the simulated results obtained by numerically integrating the nonlinear Schrodinger's equation. Specifically, the interaction between the pump, signal and

idler is described by the following propagation equations [9, 28]

$$\frac{dP_p}{dz} = -\alpha P_p - \frac{\alpha_2}{A_{\text{eff}}} (P_p + 2P_s + 2P_i) P_p - 4 \frac{\omega n_2}{c A_{\text{eff}}} P_p \sqrt{P_s P_i} \sin \theta - 2 \frac{\alpha_2}{A_{\text{eff}}} P_p \sqrt{P_s P_i} \cos \theta \quad (3a)$$

$$\frac{dP_s}{dz} = -\alpha P_s - \frac{\alpha_2}{A_{\text{eff}}} (2P_p + P_s + 2P_i) P_s + 2 \frac{\omega n_2}{c A_{\text{eff}}} P_p \sqrt{P_s P_i} \sin \theta - \frac{\alpha_2}{A_{\text{eff}}} P_p \sqrt{P_s P_i} \cos \theta \quad (3b)$$

$$\frac{dP_i}{dz} = -\alpha P_i - \frac{\alpha_2}{A_{\text{eff}}} (2P_p + 2P_s + P_i) P_i + 2 \frac{\omega n_2}{c A_{\text{eff}}} P_p \sqrt{P_s P_i} \sin \theta - \frac{\alpha_2}{A_{\text{eff}}} P_p \sqrt{P_s P_i} \cos \theta \quad (3c)$$

$$\begin{aligned} \frac{d\theta}{dz} = & (k_s + k_i - 2k_p) + \frac{\omega n_2}{c A_{\text{eff}}} (2P_p - P_s - P_i) \\ & + \frac{\omega n_2}{c A_{\text{eff}}} \left(P_p \sqrt{\frac{P_s}{P_i}} + P_p \sqrt{\frac{P_i}{P_s}} - 4\sqrt{P_s P_i} \right) \cos \theta + \frac{\alpha_2}{A_{\text{eff}}} \left(P_p \sqrt{\frac{P_s}{P_i}} + P_p \sqrt{\frac{P_i}{P_s}} - 4\sqrt{P_s P_i} \right) \sin \theta \end{aligned} \quad (3d)$$

where P_m and k_m , $m = \{p, s, i\}$ represent the powers and propagation constants of the pump, signal and idler waves, α is the linear loss coefficient, ω is the optical center frequency, c is the speed of light in vacuum, n_2 is the optical Kerr coefficient, α_2 is the TPA coefficient, and $\theta(z)$ represents the local phase mismatch. On the RHS of Eqs. (3a)–(3c), the second term corresponds to degenerate and non-degenerate TPA. The third and the fourth terms correspond to FWM contributed from the real and imaginary parts of the third-order nonlinear susceptibility $\chi^{(3)}$. These last two terms are also responsible for the power transfer between the interacting signals, governed by the phase relation $\theta(z)$. If the idler wave is absent at the input facet, this phase relationship has an initial value $\theta(0) = \pi/2$ [28]. In the phase-matched condition, the sum of first and second terms on the RHS of Eq. (3d) is zero and $\theta(z)$ stays $\pi/2$. In this condition, the power is efficiently transferred from the pump to the signal and the idler. In the non-phase-matched conditions, $\theta(z)$ deviates from $\pi/2$ and the power can transfer from the signal and idler to the pump, which reduces FWM conversion efficiency. For the intensities explored here, the induced fifth-order nonlinear refractive change and three-photon absorption were not observed and therefore, their effects are not included in Eqs. (3a)–(3d).

The dominant contributions in the local phase mismatch are the dispersion-length product of the waveguide and the nonlinear phase change. For these waveguides, the nonlinear phase change is determined by the Kerr effect since the TPA coefficients are negligibly small. The group-velocity dispersion is determined by a combination of material and modal dispersion that are determined by the alloys used in the heterostructure and the waveguide shape. Characterizing the FWM conversion efficiency with small wavelength detuning, linear loss measurements, and nonlinear loss tangent allow the model fits of the data in Fig. 5 to determine the GVD of the waveguide. These measurements of the FWM conversion efficiency as a function of detuning wavelength, $\Delta\lambda$, is therefore used to determine the GVD of the coated waveguide to be +0.44 ps²/nm, and +0.22 ps²/nm for the same waveguide after SiN_x has been preferentially removed.

Measurements of several waveguides patterned by refloned photoresist of different widths were analyzed in this manner. Figure 6 summarizes these experiments along with simulations of the GVD for both TE and TM modes as a function of waveguide width for a variety of waveguides sidewall coatings. The GVD of the TE polarization mode was measured when the input polarization state of pump and signal were adjusted to excite only the TE mode of the waveguides. In the same way, the GVD of the TM polarization mode was measured when the input polarization state of pump and signal were adjusted to excite only the TM mode of the waveguides. Independent measurements of the SiN_x indicate an index of refraction of 1.86 and

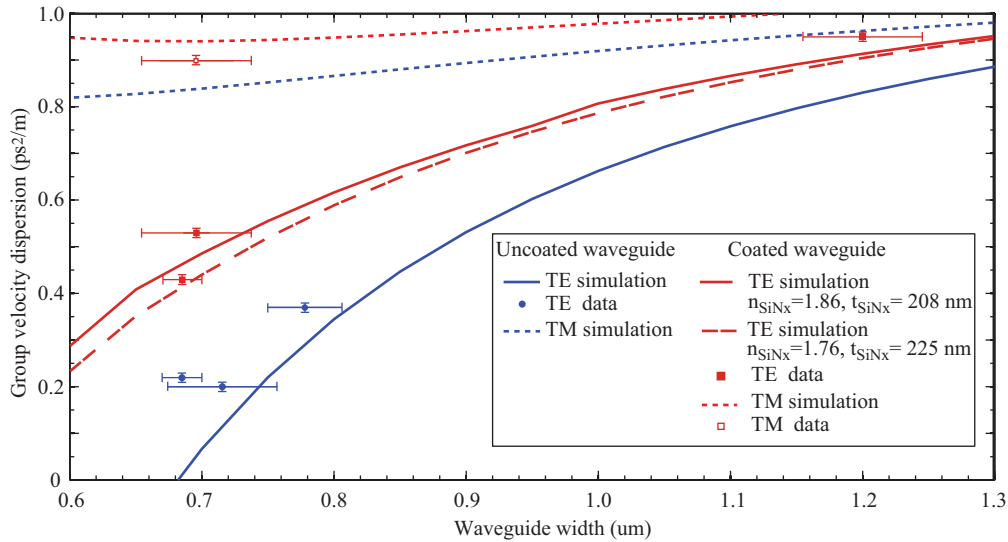


Fig. 6. Measured and simulated group velocity dispersion as a function of waveguide width for the TE and TM waveguide modes of waveguides fabricated with a conformal SiN_x coating, and the TE mode of waveguides without SiN_x coating. All waveguides have anti-reflection coatings and are evaluated at a wavelength of 1550 nm.

sidewall thickness of 225 nm. It is important to note that the actual physical parameters of the SiN_x coating are not routinely measured on waveguide devices that demonstrate low facet reflectivity. Additionally, the estimated facet reflection from a SiN_x coating with these parameters is higher than the facet reflectivity that is verified for each waveguide. Two curves are therefore shown in Fig. 6 (solid red and double-dash red) that represent reasonable variations in the index of refraction and SiN_x thickness that produce perfect anti-reflection coatings. Through extensive evaluation using plan-view scanning electron microscopy, it has been found that the actual waveguide width varies with a very long period along the length of the waveguide. The length scale of this variation is significantly longer than the optical wavelength and therefore does not influence the optical scattering loss. The observed variation is represented as horizontal error bars in Fig. 6, and varies from waveguide to waveguide. One example is the $0.69\text{-}\mu\text{m}$ wide waveguide that has a measured width variation of ± 45 nm. This slow variation of the waveguide width could affect the GVD plot versus waveguide width because the several point width assessment completed here is insufficient to determine the true mean and standard deviation of the entire waveguide.

The simulation results of the waveguides are in good agreement with the experimental results from TE and TM modes, with the exception of one of the uncoated waveguides. For this sample, it is likely that the SiN_x was not completely removed and a small region of residual SiN_x causes the unexpected increase in the measured GVD. From these results it is apparent that the conformal SiN_x that is necessary as anti-reflection coatings on the input and output facets negatively impacts the GVD, and that the highest bandwidth waveguides are those with low GVD and no dielectric coatings on the waveguide sidewalls.

5. Conclusions

Engineering the fabrication process of sub-micron modal area AlGaAs nonlinear optical waveguides enables efficiency and bandwidth improvements in continuous-wave-four-wave mixing

conversion. The reduction in propagation loss in the waveguide by plasma-assisted reflow process, and selective removal of dielectric coatings from the waveguide sidewalls prove to be key innovations for achieving the high conversion efficiency and large 3-dB bandwidth in waveguides that show no measurable impact of two photon absorption.